Monthly Notices
of the
ROYAL ASTRONOMICAL SOCIETY

MNRAS **457,** 1410–1418 (2016) doi:10.1093/mnras/stw045

High-angular-resolution stellar imaging with occultations from the *Cassini* spacecraft – III. Mira

Paul N. Stewart,[1]★ Peter G. Tuthill,[1] Philip D. Nicholson[2] and Matthew M. Hedman[3]

[1]*Sydney Institute for Astronomy, School of Physics, The University of Sydney, NSW 2006, Australia*
[2]*Department of Astronomy, Cornell University, Ithaca, NY 14853, USA*
[3]*Department of Physics, University of Idaho, Moscow, ID 83844, USA*

Accepted 2016 January 6. Received 2016 January 6; in original form 2015 July 22

ABSTRACT

We present an analysis of spectral and spatial data of Mira obtained by the *Cassini* spacecraft, which not only observed the star's spectra over a broad range of near-infrared wavelengths, but was also able to obtain high-resolution spatial information by watching the star pass behind Saturn's rings. The observed spectral range of 1–5 microns reveals the stellar atmosphere in the crucial water-bands which are unavailable to terrestrial observers, and the simultaneous spatial sampling allows the origin of spectral features to be located in the stellar environment. Models are fitted to the data, revealing the spectral and spatial structure of molecular layers surrounding the star. High-resolution imagery is recovered revealing the layered and asymmetric nature of the stellar atmosphere. The observational data set is also used to confront the state-of-the-art cool opacity-sampling dynamic extended atmosphere models of Mira variables through a detailed spectral and spatial comparison, revealing in general a good agreement with some specific departures corresponding to particular spectral features.

Key words: stars: AGB and post-AGB – circumstellar matter – stars: individual: IRC+10216 – stars: oscillations – stars: winds, outflows – infrared: stars.

1 INTRODUCTION

The archetype of the 'Mira-type' variables, Mira (aka o Ceti, or HD 14386), was the first identified intrinsically variable star and after centuries of research it remains an intensively studied object today. It is an M-type (oxygen rich) asymptotic giant branch (AGB) star with an extraordinary 8 mag pulsation amplitude at visible wavelengths and a pulsation period of 331 d (Mayer et al. 2011). The star is known to be experiencing significant mass-loss of around $10^{-7}\,M_{\odot}\,yr^{-1}$ (Mauron & Caux 1992). Measurements of the distance to the star range from 92 (van Leeuwen 2007) to 107 parsecs (Knapp et al. 2003).

For C-type (carbon-rich) Mira variables, physical processes which produce mass-loss emerge readily from model stellar atmospheres. Matter is elevated by radial pulsations of the star and as this cools carbonaceous dust grains are able to condense. Due to the opacity of these grains, they are easily able to be radiatively accelerated outwards through absorption of stellar photons, also entraining atmospheric gas and producing an outflowing wind (Winters et al. 2000; Sacuto et al. 2010; Nowotny et al. 2011). A similar physical process has been sought to explain the winds of M-type Mira variables, but models have yet to produce a convincing wind using dust absorption, due in a large part to the relative lack of opacity of modelled silicate dust grains. Höfner (2008) suggested that the wind could instead be produced by micron-scale transparent grains which scatter the stellar photons, and a signature of such grains was detected by Norris et al. (2012) using polarimetric interferometry. The Cool Opacity-sampling Dynamic EXtended (CODEX) atmosphere models presented in Ireland, Scholz & Wood (2008, 2011) and Scholz, Ireland & Wood (2014) aim to simulate the physical behaviour of the atmospheres of M-type Mira variables. These models have been shown to reproduce some spatial and spectral features of such stars (Ireland et al. 2008, 2011).

A significant hurdle in unravelling the nature of the stellar atmosphere in which these winds form has been obtaining concurrent observational data with both fine angular sampling and spectral coverage. This difficulty is enhanced by telluric atmospheric absorption in the near-infrared due to the presence of water vapour. These same water-bands are also known to be very significant features in the atmosphere of Mira type stars (Matsuura et al. 2002). The timing of maximal brightness within each stellar pulsation is a function of wavelength, with visual bands preceding the infrared. The minima are known to be wavelength independent (Lockwood & Wing 1971).

In this paper, we present spectral measurements and observations of Mira as it is occulted by the rings of Saturn. The use of *Cassini* occultations for stellar imaging was detailed in Stewart et al. (2013, hereafter Paper I) who demonstrated their potential for simultaneous spectral and high spatial resolution studies. This work was extended

★E-mail: p.stewart@physics.usyd.edu.au

to demonstrate how the technique could be combined with tomographic image reconstruction to produce high-resolution 2D images of stellar targets in Stewart et al. (2015b, hereafter Paper II), with images produced using the technique presented in Stewart et al. (2015c). The spectral window which is open to the infrared channel of *Cassini* 's Visible and Infrared Mapping Spectrometer (VIMS-IR) ranges from 0.8 to 5.1 μm, providing access to the otherwise inaccessible water-band regions in the circumstellar environment. The recovery of stellar spectra from VIMS-IR is detailed in Stewart et al. (2015a) which was used to produce the *Cassini* Atlas Of Stellar Spectra (henceforth CAOSS). Paper I showed that Mira's faint companion is not detectable in these data with the short exposure times used.

We provide details of the observations in Section 2, and then examine the measured spectral structure of the star in Section 3, and the spatial structure of the circumstellar environment in Section 4. A detailed comparison of the observations with the state-of-the-art CODEX models is performed in Section 5.

2 THE OBSERVATIONS

Observations of Mira for which spectra could be recovered are given in Table 1. A subset of these also contains suitable ring edge occultations permitting spatial structure recovery, as listed in Table 2.

The spectral observations were acquired in two different ways depending on the intended purpose of the observation. Epochs 2 and 14 were obtained as part of an ongoing instrumental calibration and monitoring programme as detailed in Stewart et al. (2015a), whilst all other epochs were acquired as part of a stellar occultation observation. The occultation observations were initially acquired in order to understand the structure of Saturn's rings. Results from these studies were first published by Hedman et al. (2007) revealing the presence of self-gravity wake structures within the A ring. Papers I and II demonstrate that it is also possible to recover details of the circumstellar environment from such observations. Stellar occultations were observed on six separate orbits in which Mira passed behind the rings from the perspective of *Cassini* . Of these, three had geometries suitable for recovery of spatial information and are detailed in Table 2. Two of the geometries (10a & 10b) were unsuitable due to the high velocity of the spacecraft at the time of the observations. In the observation labelled 5d, the occultation chord passed through the F ring only, and did not intersect any sharp edges suitable for our purpose. The edges listed in Table 2 are those found to produce light curves suitable for model fitting. The sharpness of these edges has been measured by Colwell et al. (2010) and Jerousek, Colwell & Esposito (2011) to be as small as 9.0 m radially in the ring-plane, corresponding to an angle of 1.2 mas for a typical occultation geometry. This is considerably smaller than the perpendicular sampling resolution (θ_S) observations in this set (Table 2). This edge sharpness is further enhanced by the very small opening angle (3.°45) between the ring-plane and the line of sight to the star, resulting in rings that are almost edge on to the line of sight, and causing the rings to be almost opaque. It has been established in Paper I that such geometries are particularly favourable to the recovery of stellar spatial information.

The point where the line of sight from *Cassini* to the star is intercepted by the planetary ring-plane is referred to as the Ring-Plane Intercept (RPI) as defined in Paper I. The spatial sampling resolution of each occultation event (θ_S) is dependent on the observation parameters of the instrument, the orbital geometry of Cassini, and the speed at which the RPI moves in the direction perpendicular to the occulting edge as detailed in Paper I. The value of θ_S for each of the occultation events used in this paper are listed in Table 2. The position angle (PA) of each edge is defined by the angle between the outward-directed normal to the ring edge in *Cassini*'s sky-plane, and a projection of the terrestrial 'north' originating from the RPI. This angle is the direction in which the image of the star in the sky-plane is sliced by the occultation process, and allows for comparisons to other methods in the literature reported

Table 1. Spectral observations. Epoch identifies each observation based on the year that were acquired. Visual pulsation phase (ϕ) is measured relative to the adjacent peaks in the visual band based on measurements in the AAVSO data base. Each oscillation is defined to be divided evenly in time spanning 0 to 1, with the visual maximum occurring on the whole number. The relative uncertainties of phase are within ±0.01 whilst their absolute uncertainties are ±0.05. The cycle is identified by the epoch label and by whole numbers in ϕ where $\phi = 0.0$ is the 2001 September 10.

Epoch	Date	ϕ	# Channels	λ range (μm)
2	2002 Jul 19	0.94	244	0.88–5.12
5a	2005 May 24	4.03	14	0.94–2.79
			114	2.76–5.07
5b	2005 Jun 11	4.08	14	0.94–2.79
			118	2.76–5.12
5c	2005 Jun 18	4.14	14	0.94–2.79
			117	2.76–5.11
5d	2005 Aug 05	4.25	14	0.94–2.79
			116	2.76–5.12
10a	2010 Jun 03	9.57	155	0.88–3.19
10b	2010 Jul 24	9.72	14	0.94–2.79
			114	2.76–5.11
14	2014 Apr 11	13.79	246	0.88–5.12

Table 2. Spatial observations from stellar occultations. Epoch identifies each observation as per Table 1. Edge is the name of the ring, ringlet, or gap edge which has occulted the star. θ_S is the sampling resolution at each edge. PA is the position angle of the occultation in Earth-based celestial coordinates with north being 0°. The names of edges are as defined by Colwell et al. (2009) with identifiers from French (1993) where 'IEG' and 'OER' indicated the inner and outer edges, of gaps or rings/ringlets, respectively. Each edge is crossed in both the ingress and egress of the occultation, providing the two different values in the θ_S and PA columns in temporal order.

Epoch	Date	Edge	θ_S(mas)	PA(°)
5a	2005 May 24	A OER	11.9/7.00	7/175
		Keeler OEG	11.9/7.00	7/175
		Keeler IEG	11.9/6.99	7/175
		Encke OEG	12.1/6.91	7/175
		Encke IEG	12.1/6.91	8/175
		Laplace IER	15.6/5.97	20/172
		Huygens OER	18.9/5.41	34/170
		Huygens IER	19.0/5.39	35/170
		B OER	19.5/5.34	37/170
5b	2005 Jun 11	A OER	13.7/6.67	12/174
		Keeler OEG	13.7/6.65	12/173
		Keeler IEG	13.8/6.65	12/173
		Encke OEG	14.6/6.42	15/173
		Encke IEG	14.8/6.38	16/170
5c	2005 Jun 29	A OER	17.1/6.00	24/171
		Keeler OEG	17.4/5.95	25/171
		Keeler IEG	17.5/5.95	25/171
		Encke OEG	22.6/4.92	64/168
		Encke IEG	22.1/4.69	77/169

in a terrestrial reference frame. The technique applied to calculate the PA is detailed in Section 2 of Paper II.

3 VIMS-IR SPECTRA

Spectra of Mira have been recorded by VIMS with different configurations on eight different occasions and are presented in Fig. 1. The resultant spectra for each epoch vary in both spectral coverage and resolution. Epochs 2 and 14 are from CAOSS and of these, 14 comes directly from the main atlas with a well calibrated absolute flux and is shown in blue in the bottom panel of Fig. 1. Epoch 2 in the top panel of Fig. 1, also shown in blue, has a potentially unreliable absolute flux calibration and must be treated with caution. However, its relative calibration over small ranges in wavelength is acceptable. The uncertainty in absolute flux calibration is due to part of the stellar image falling between the instrument's pixels and is discussed in detail in Stewart et al. (2015a). The purple spectra in the other panels come from single frames taken in 2D imaging mode before each occultation observation. These were acquired in order to identify in which pixel within the image the star is located and are presented for epochs 5a–d and 10b, but not for 10a where the finding frame was noise dominated. Early in the mission, these finding frames only consisted of specific parts of the spectrum in order to avoid potential scattered light from the rings, and are consequently limited to the red end of the spectral range. They have been processed following standard protocols used to produce CAOSS in order to recover flux-calibrated spectra. The black points in Fig. 1 come from the occultation observations themselves. They are single-pixel measurements extracted from the ends of the occultation time series data, either before or after the line of sight is intercepted by the F ring, and therefore contain only starlight and no contamination by tenuous ring material. Occultation observations are generally recorded with the 256 spectral channels binned into 32 channels, so these are much coarser than other VIMS-IR spectra. An exception is the 10a occultation which was acquired at full spectral resolution. For comparison purposes, the brightness of Mira in three photometric bands from a single epoch published in 2MASS are shown in orange (Skrutskie et al. 2006).

3.1 Spectral structure

The dominant spectral features at all epochs are the strong absorption bands at 1.1, 1.4, and 1.9 μm, corresponding to molecular water in the stellar atmosphere (Tej et al. 2003). These are better defined for those epochs with higher spectral resolution, yet are very pronounced at all epochs. The other significant spectral feature is the broad hump which peaks between 3.5 and 4 μm. This shape of this feature is primarily determined by the relative abundances of H_2O, CO and OH (Yamamura, de Jong & Cami 1999).

3.2 Temporal variations in the spectra

Of the eight epochs for which spectra have been observed, four are on adjacent or near-adjacent orbits (5a–d), two are temporally near each other but distant from the other epochs (10a–b), and another two are temporally isolated (2 and 14). The orbital period of *Cassini* at the time of 5a–d and 10a–b was approximately 18 d – only a small fraction of Mira's 331 d stellar pulsation period.

The first epoch, 2, occurred immediately before a visual maximum as the infrared luminosity was rising.

Epochs 5a–d span 73 d, or 22 per cent of one stellar pulsation cycle, and correspond to the period immediately following visual

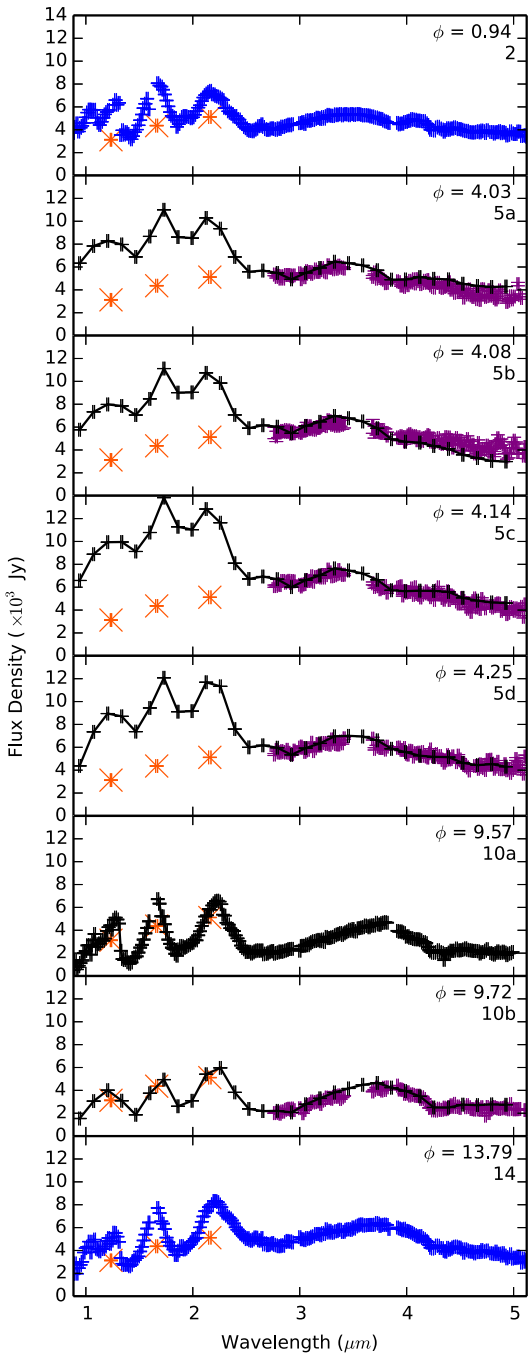

Figure 1. An eight epoch record of the changing spectrum of Mira. The visual phase and epoch label is in the top-right corner of each panel. All panels span identical axes with the horizontal showing the observed wavelength in microns and the vertical being flux density in 10^3 Janskies. Blue spectra are from CAOSS. The purple spectra are processed through the CAOSS pipeline, but come from single frames taken before an occultation observation. Black points come from the occultations themselves with the line through them given as a guide to the eye. The orange crosses in each panel are *J*, *H*, *K* fluxes from 2MASS and are shown to provide a static reference. Full details are in Section 3.

maximum. Woodruff et al. (2008) identified a phase lag of ∼0.2 behind the visual cycle for the *J*, *H* and *K* bands and ∼0.3 for *L* band. This is evident in our observations, where the maximum at *J*, *H*, and *K* are seen to occur between 5c and 5d, whilst *L* band is still rising at 5d.

Epochs 10a and 10b span 51 d near the minimum of the visual cycle, where the minima are wavelength independent and correspond to the largest angular size (Lockwood & Wing 1971). Epoch 10a has the deepest water absorption bands of all epochs with flux in the band between *H* and *K* decreased to 27 per cent of the mean of the adjacent peaks. This is as expected with the atmosphere at its largest extent and near minima in brightness (Woodruff et al. 2008). This epoch also shows a shift in the peak of the broad hump towards longer wavelengths as OH becomes more abundant. When down-sampled to a matching spectral resolution, the differences between 10a and 10b are found to be very small, confirming that the dimmest parts of the pulsation cycle can be relatively stable over short time-scales of the order of 15 per cent of a pulsation cycle.

The final epoch, 14, occurred almost 4 yr after the previous epoch and was after the visual minimum, as the star had started to brighten. The depth of the water-band between *H* and *K* reduced to 43 per cent of the adjacent peaks as the atmosphere begins to contract. The peak of the broad hump is seen to move back towards the shorter wavelengths.

4 CIRCUMSTELLAR STRUCTURE

The process to recover high-resolution spatial information from these observations is detailed in Paper I, along with the results of fitting a uniform disc model. In the following subsections, variations on this simple model are presented and demonstrated to better describe the structure of Mira's circumstellar environment. Temporal variations in this structure between epochs are explored, as are departures from spherical symmetry in the fitted models. This section concludes with the presentation of high-resolution tomographically recovered 2D images of Mira in four wavebands.

4.1 Radial structure

The uniform disc model used in Paper I was selected to allow for a direct comparison of the resolving ability of this technique to literature measurements. It assumes the star is a uniformly bright perfect circle on the sky, and has only a single free parameter, the disc diameter. Like most existing stellar models it assumes the star is spherically symmetric.

Here we extend this simple model, and upgrade the fitting algorithm to MULTINEST (Feroz et al. 2014), which improves the fitting results and provides a better indication of the real structure of Mira's circumstellar environment. The first change to the model is the addition of an optically and physically thin spherical shell, concentric with the stellar disc to produce a uniform disc with single shell (UDSS) model. Similar structures have been previously identified enveloping Mira variables (Karovicova et al. 2011; Wittkowski et al. 2011), including Mira itself (Lopez et al. 1997; Cruzalebes et al. 1998). The results of this model fit with a comparison to the uniform disc model used in Paper I and spanning all observed wavelengths and three spatial epochs are shown in Fig. 2. The curves shown in this figure are the average of the fitted parameters for all occulting edges at that epoch, in effect averaging over PA and assuming spherical symmetry.

The reduced χ^2 plots (green and blue lines in the lower panels of each set) show that the UDSS model is a significantly better fit

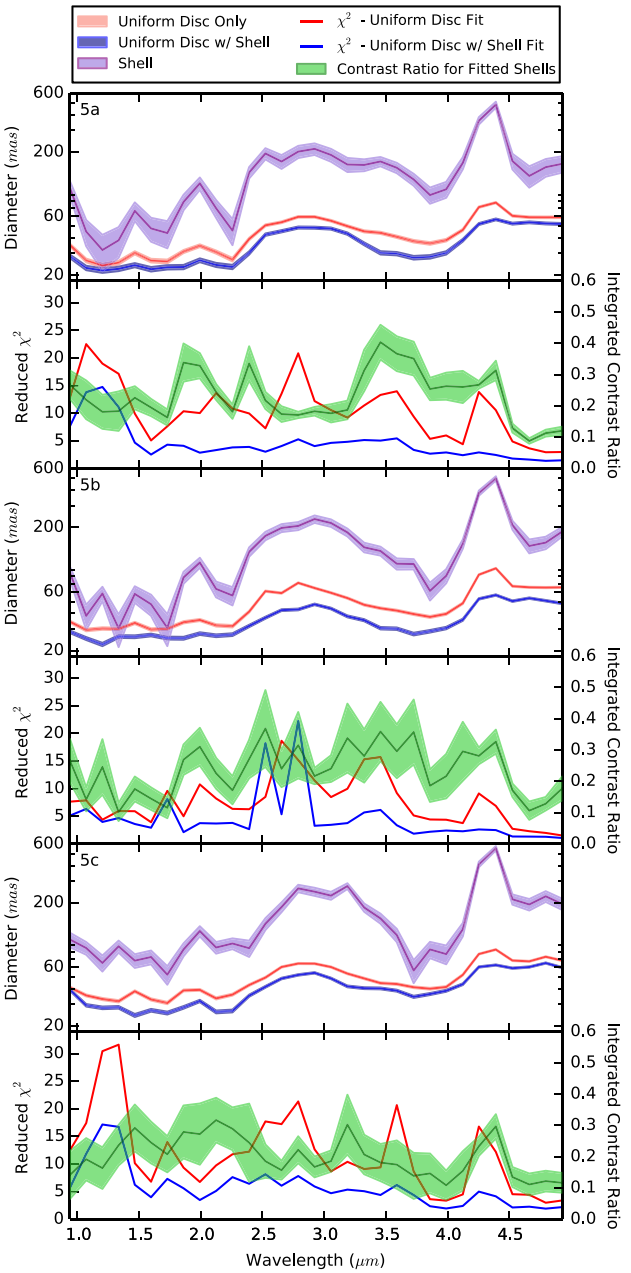

Figure 2. The uniform disc and UDSS model fits for the three spatial epochs. Each epoch is the average of all suitable occulting edges observed within that occultation as listed in Table 2. 5a is shown in the first two panels, followed by 5b in the middle two and 5c in the lower two panels. The upper panel in each pair shows the diameters of modelled stellar structure versus wavelength with green indicating the size of a fitted uniform disc model without a shell, and blue representing the diameters of the uniform disc with a thin spherical circumstellar shell in the UDSS model. The smaller of these is the disc, whilst the larger is the shell. The filled region represents a 1σ variation in model fits. The lower panel in each set shows the reduced χ^2 for the uniform disc fit and the UDSS fit in green and blue, respectively, against the left axis. The lower panel in each set also shows the integrated contrast ratio of all shell flux to all disc flux with 1σ uncertainties in purple against the right axis.

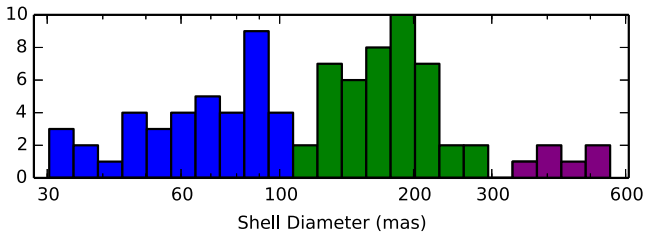

Figure 3. A histogram revealing the distribution of fitted shell diameters. The horizontal axis shows the shell diameter in milliarcseconds and the vertical axis shows the number of fitted values in each bin. These values are the measured shell diameter for all spectral channels at all epochs. The data are presented in three colours identifying the structures discussed in Section 4.1.

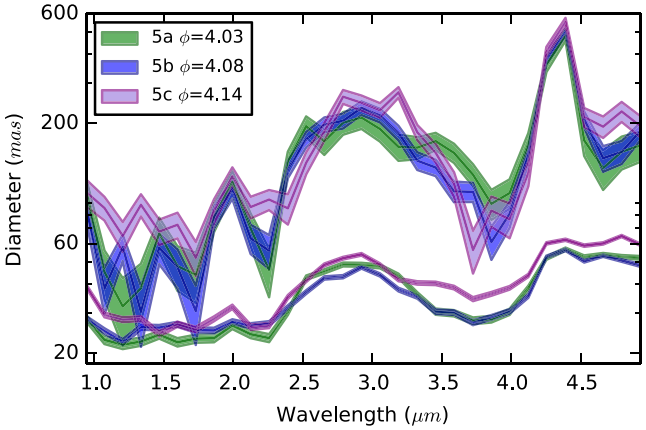

Figure 4. The UDSS model as shown in Fig. 2. The lower curves are the diameters of the fitted uniform disc whilst the upper are the fitted diameters of the shell. All three epochs are shown on the same axes to emphasize the temporal changes in the circumstellar environment. The epochs are labelled in the legend and coloured in green for 5a, blue for 5b, and purple for 5c. Each curve is comprised of a centreline within a shaded region. The centreline indicates the parameters which result in the best fit in each spectral channel, whilst the shaded region represents the 1σ variation to these best-fitting parameters.

to the observations across almost all wavelengths and all epochs than the uniform disc by itself. As the UDSS model contains more degrees of freedom than the uniform disc model, the reduced χ^2 provides a conservative way to illustrate the change in the quality of the fit. All epochs show the same general shape for the wavelength dependence of the disc and shell diameters. The shell tends to follow a generally similar profile to the disc, and falls into three wavelength dependent discrete levels, emphasized in the histogram shown in Fig. 3. These atmospheric layers are observed at diameters of ∼60, ∼200 and ∼400 mas and are due to absorption and emission by different molecular species dominating at different temperatures. The layers are identified as corresponding to H_2O at 2000 K, H_2O at 1200 K, and CO_2 at 800 K, respectively (Yamamura et al. 1999; Tej et al. 2003; Justtanont et al. 2004). Other molecular species have previously been shown to contribute to the flux in the near-infrared, such as CO, OH, SiO, and C_2H_2 (Yamamura et al. 1999; Tej et al. 2003; Justtanont et al. 2004; van Loon et al. 2006; Wittkowski et al. 2011). However, spectral features corresponding to these species were not observed within this data set. Fluctuations in the size of the inner, hotter, layer correspond to the water-bands identified spectrally in Section 3. The integrated contrast ratio between the shell and the disc (filled band in the lower panels of each set) is broadly constant. Redwards of ∼4.5 μm, the contrast ratio in all epochs drops to a steady 10 per cent, but otherwise tends to fluctuate between 20 and 30 per cent across the observed wavelength range.

These molecular layers are observed as a relative increase in atmospheric opacity in the vicinity of the listed diameters. The inner layer, H_2O at 2000 K, is associated with the dissociation of H_2O molecules, whilst the other two identified layers indicate an accumulation of molecular material at their respective diameters. The layers are expected to be dynamic and transient features, oscillating with the stellar pulsations, and expanding outward with the stellar wind.

Due to the detection of physical circumstellar shells with discrete diameters, more complex models were fitted with nested shells, and nested uniform and limb darkened discs. The results were a marginally yet consistently improved reduced χ^2 value for most wavelengths in all epochs. This improvement was not significant enough for any of these models to be able to definitively state the superiority of any particular model, but it does support the idea of a multilayered atmosphere. The UDSS model used here is a simplification of the circumstellar structure. In spite of this, it is shown to be highly effective at identifying the spatial location of broad molecular features previously identified spectrally.

4.2 Temporal variations in circumstellar structure

Our three spatial epochs were recorded on subsequent orbits with a constant temporal separation of approximately 18 d. The epochs are therefore separated by approximately 0.054 stellar pulsation periods, and span a total range of 0.11 periods based on a 331 d stellar period. We determined that these observations correspond to phases of $\phi = 4.03$, 4.08 and 4.14 for epochs 5a, 5b and 5c, respectively, where $\phi = 4.0$ is the preceding visual brightness maximum. This corresponds to the region between the visual and near-infrared maxima ($\phi = 0.2$). Mira variables have long been shown to exhibit a coarse anticorrelation between their visible luminosity and angular diameter (Burns et al. 1998; Young et al. 2000; Thompson, Creech-Eakman & Akeson 2002; Woodruff et al. 2009). The brightest parts of Mira's pulsation cycle occur when the star is near its smallest physical extent and exhibits less molecular absorption. This is particularly true for the photosphere and inner regions of the atmosphere where the vast majority of the flux originates. Oscillations in the distant outer layers of the atmosphere span many periods of the photospheric cycle, and contribute to the observed cycle to cycle variations.

Fig. 4 shows the diameter changes in fitted UDSS models between epochs 5a, 5b and 5c. This allows for any variations between epochs to be easily identified. There are two regions where there appears to be very little difference in the shell diameters between the three epochs. These are one of the water-bands, between 1.8 and 2.2 μm and the CO_2 feature at 4.4 μm, suggesting these structures can be quite stable over the short term. Epochs 5a and 5b are mostly very similar, with a slight decrease in the shell size between 3.4 and 4.1 μm, revealing the star passing through it is minimum in size. The most significant temporal change observed is an expansion between 5b and 5c in most wavelengths for both the disc and the shell. This effect is notable at wavelengths shortward of 1.7 μm and longward of 4.5 μm for the shell. It is also seen in the disc diameters for all wavelengths longer than 3.3 μm.

Woodruff et al. (2008) presented fitted sinusoidal phase curves of Mira for a uniform disc model in the *J*, *H*, *K*, and *L* bands.

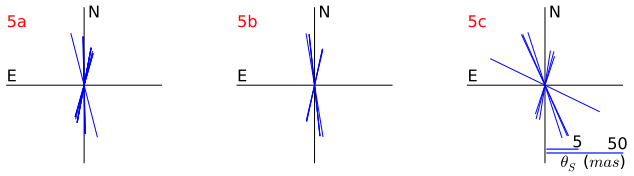

Figure 5. Angular diversity roses as defined in Paper II, showing the PA sampled by each edge within the occultation. The lengths of the lines are proportional to $\log(v_\perp)$ (the perpendicular velocity of the RPI in *Cassini*'s sky-plane) and give an indication of how the sampling resolution changes with angle with a shorter line indicating a finer sampling resolution. These lengths can be compared to the scale in the bottom-right corner of the plot, or taken from Table 2. Note that the diversity of sampled angles in 5b is particularly poor whilst 5c is substantially more diverse. North is the top of each plot with east to the left.

The behaviour at *J*, *H* and *L* band in our observations is consistent with their fitted sinusoids. *K* band (2.26 μm) however, was expected to have a decrease in uniform disc diameter of approximately 10 per cent over the course of the three epochs which is not evident in the observations, in either the disc or shell.

4.3 Asymmetry

The models discussed above assume that the star is inherently spherically symmetric. There have been very few stellar models to date which have tried to incorporate departures from simple symmetric structure (Woitke 2006a,b). This is in sharp contrast to the wealth of observational data which reveal significant asymmetries in Mira variable stars (Lopez et al. 1997; Chandler et al. 2007), including Mira itself (Karovska et al. 1997; Martin et al. 2007).

Each occulting edge is associated with a specific angle, and the associated brightness profile encodes spatial information about the image of the star projected on a single direction. The occulting angles for these observations are listed in Table 2 and angular diversity roses showing the relative PA of these slices are shown in Fig. 5. By comparing the estimated size of circumstellar structure recovered from different occulting edges, it is possible to determine the extent of any deviations from circular symmetry present at the time of the observations. This technique is limited to measuring asymmetry spanned by the diversity of PA available. Fig. 5 reveals that epochs 5a and 5b lack sufficient angular diversity to make any substantial claims about any asymmetries at these epochs. But epoch 5c does have sufficient diversity to observe such asymmetries, and these will be explored in Section 4.4.

4.4 Kronocyclic tomography

Paper II demonstrated how these *Cassini* observations of stellar occultations can be used to recover high-resolution 2D images of the target star and its circumstellar environment. This is done by fitting model-independent brightness profiles to data for a range of occultation angles and combining them tomographically to produce a 2D image of the star. The relatively good angular diversity of epoch 5c, as discussed in Section 4.3, allows the application of this method and the recovery of stellar images in different wavebands. These are shown in Fig. 6 for four diverse spectral bands. Five adjacent spectral channels were co-added for the recovery of the model-independent brightness profiles in order to suppress noisy data points which can easily lead to significant artefacts in the resultant image. This results in a broad spectral bandwidth of ∼0.68 μm for each image, with the centre wavelength indicated in the top-left corner of each panel. These broad-bands were selected to emphasize the identified circumstellar features. No imaging data were found in the literature with which to directly compare these recovered images. In order for a comparison to be meaningful, observations must be in similar spectral bands and from proximate epochs. The nearest matches in the literature are a 700 nm image from an observation in 1991 (Wilson et al. 1992) and a 500 nm image from 1995 (Karovska et al. 1997). In spite of the elapsed decade between these and the 2005 epoch presented here, and observing in a different part of the spectrum, a similar broad northern/north-western extension observed in these earlier images is seen in the shortest wavelength image presented in Panel 1 of Fig. 6.

The general spectral shape seen in the shell and disc of 5c in Fig. 2 is seen in the variation in brightness of the structures between the different spectral bands in Fig. 6, with a larger size at $\lambda = 2.92$ and 4.53 μm and a smaller size through the water-bands at $\lambda = 1.32$ μm, and at $\lambda = 3.86$ μm. The discrete shell levels at ∼60, ∼200 and ∼400 mas described in Section 4.1 are evident to some extent in all bands, but are particularly clear at $\lambda = 2.92$ and 4.53 μm. The outer shell is asymmetric, clumpy, and incomplete in most bands, with the exception of 4.53 μm. The faint north-westward protrusion in the recovered images at 1.34, 2.92, and 3.86 μm is a tomographic artefact as discussed in Paper II. There is a broad asymmetric brightening to the south in all bands, and there is much less structure evident in the north-west of the circum. The stellar disc itself is buried in the inner regions of the images, and is not clearly discernible.

5 CODEX MODELS

The intention of the CODEX models is to understand the cycle to cycle behaviour or Mira variables. This is done through calculations of the physical centre-to-limb profiles revealing changing temperature, and chemical and radiative states as a function of radius. The CODEX models span several stellar pulsation cycles and deliberately include cycles which are both particularly compact and extended as well as molecular layers and expanding shock driven shells. They span the range from the inner regions of the star adjacent to the stellar core, out to many stellar diameters beyond the photosphere.

The models can therefore predict structure on the spatial scales resolved in Section 4, and spectral variations throughout the spectral range covered by VIMS and discussed in Section 3. Ireland et al. (2008, 2011) compared these models to ground-based observations of the stellar spectra of the modelled stars, but did not include the near-infrared water-bands which are inaccessible to terrestrial observers. Yet these bands are critical in understanding the behaviour of these stars with their complex molecular atmospheres. The 'o54' model series is used here as it was specifically designed to closely match the observable behaviour of Mira itself. The zero-point of the pulsation phase of the CODEX model is set to an estimated maximum bolometric luminosity (Ireland et al. 2008), which lags the visual phase by approximately $\phi = 0.1$ (Ireland et al. 2004). In this analysis, the phases of the CODEX models have been shifted to the more common visual maximum at $\phi = 0.0$. The models are available divided temporally into tenths of a cycle, allowing a comparison of observations to the nearest 0.1 of a cycle. They are also generated and made public at a spectral resolution of $R \approx 1000$, but are downsampled here for the purposes of comparison with *Cassini* occultation data.

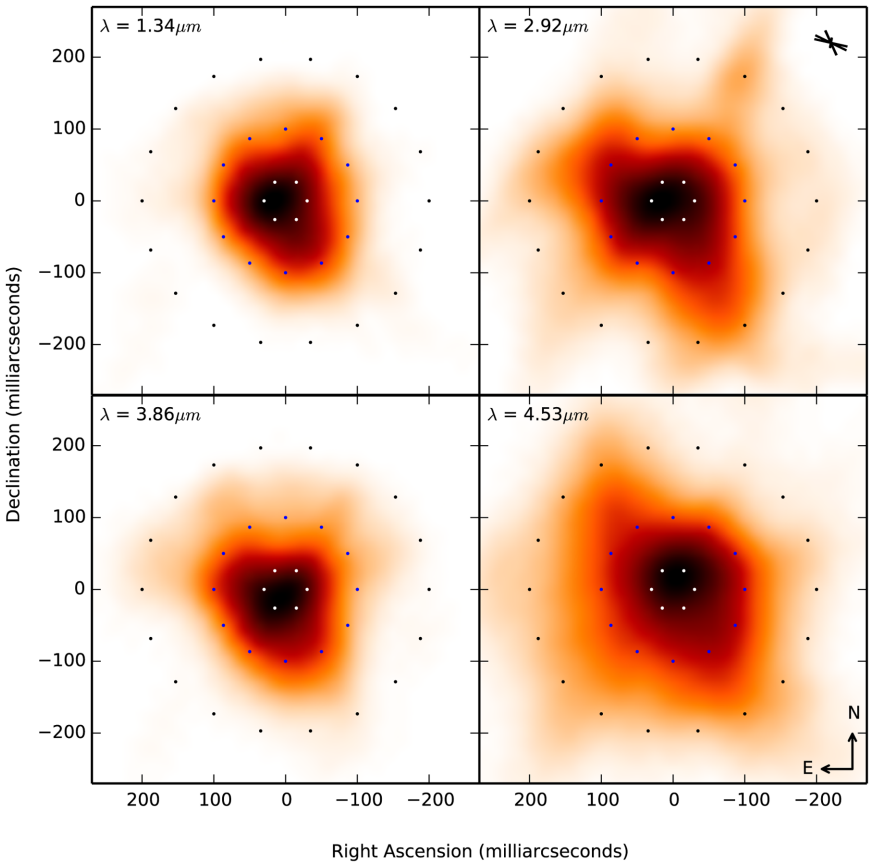

Figure 6. Tomographically recovered images of Mira in four spectral bands from the 5c epoch. The axes for all panels are identical, scaled as milliarcseconds in right ascension or declination. The centre wavelength is indicated in the top left of each panel. The angular diversity rose in the top right of the figure shows the occultation angles, and sampling resolution of the occultations used in the recovery of these images. Diameters of the 60, 200, and 400 mas shells are indicated by the circles traced by the white, blue, and black points. North is to the top and east is to the left.

5.1 CODEX spectral predictions

Fig. 7 shows the eight spectral epochs presented in Section 3 compared with the CODEX models for the nearest three phase increments. The CODEX spectra are plotted in darkening shades of red as they advance in time. For example, the 5b spectrum is compared to CODEX models for $\phi = 0.0$, 0.1, and 0.2.

The most striking variation between the spectra predicted by the CODEX models and the observations presented here occurs in 5a–d, spanning the visual and infrared peaks shortward of $\lambda = 3$ μm. In these phases, the models predict the effective elimination of the water absorption bands shortward of 2.4 μm, yet the observations show they remain, even if somewhat weaker than in other parts of the cycle. It is a possibility that the particular cycle in which these observations were acquired included an uncharacteristically dim maximum, with unusually deep water absorption bands, but AAVSO measurements in the visual band do not support this. Instead, it appears that the CODEX models underpredict the amount of H_2O absorption which occurs through the visual peak of the stellar pulsation cycle. Observations 10a–b also reveal an overpredicted CODEX luminosity around the location of the water-bands, yet the depth of the bands is approximately at the observed level. In the observations which occur between the minima and maxima (epochs 2 and 14), the predictions of the models closely match the observations for most of the covered wavelength range.

The shape of the broad dip and rise between 2.6 and 4.1 μm is well matched in epochs 14, and 10b, whilst the epoch 14 observation shows less absorption. Epochs 5a–d are seen to depart from the predictions for this wavelength region, with the predicted peak at 3.2 μm instead being located at 3.5 μm, suggesting the ratios between molecular species in the model are inaccurate.

All phases with suitable data are shown to be well predicted for wavelengths longer than 4.1 μm.

5.2 CODEX spatial predictions

A comparison of the spatial structure predicted by the CODEX models to the observations is shown in Fig. 8. CODEX centre-to-limb profiles are compared with the model-independent brightness profiles produced for kronocyclic tomographic image recovery in Fig. 6. The models are limited to only five times the photometric radius, with anything beyond this region being classed as the 'wind zone' (Ireland et al. 2008), whilst the observations extend much further from the star. It is important to note that the behaviour of the outer reaches of the CODEX models are generally decoupled from the pulsation period, with chaotic long-term trends spanning several cycles. For this reason, strict phase matching for outer structure is somewhat arbitrary, however, these longer term trends are encompassed within the limited phases range used here.

The CODEX profiles in Fig. 8 show two steep decreases. The shorter of these is observed in all four wavelengths and corresponds approximately with the inner H_2O layer identified in Section 4.1. The outer decrease occurs towards the limit of the models. At 2.92

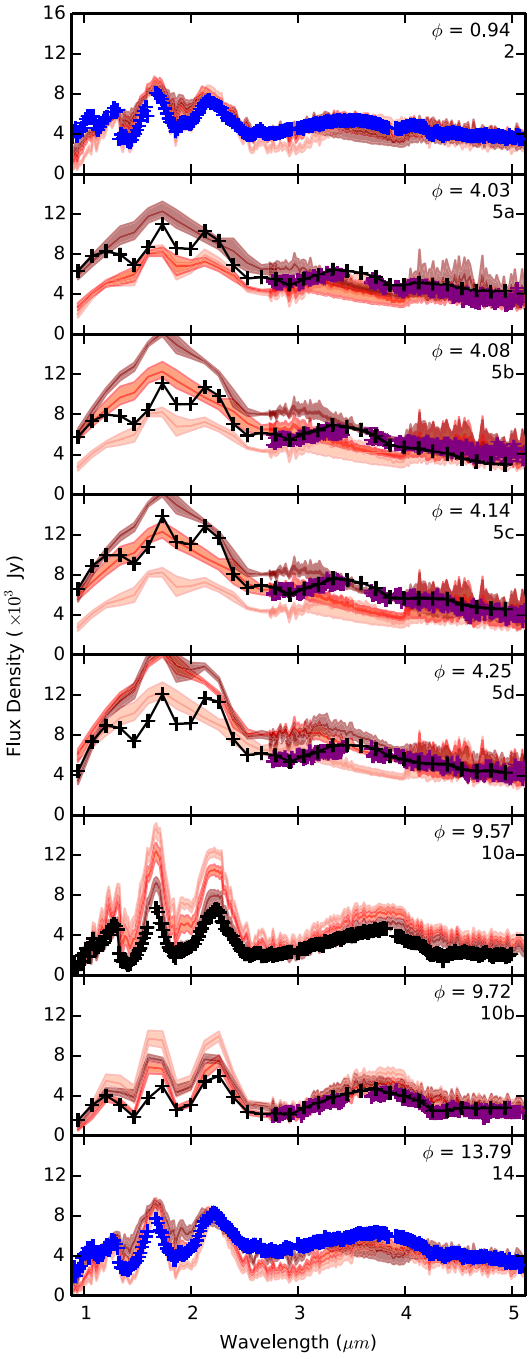

Figure 7. A comparison of CODEX spectra to *Cassini* observations. The *Cassini* observations are as described in Fig. 1. CODEX spectra are shown in three shades of red for three phases, advancing in time as colour darkens. The central of these is the nearest tenth of a cycle to each epoch, with the others being the preceding and trailing tenth of a phase. The vertical width of the CODEX spectra encompasses cycle to cycle variations including both compact and extended cycles as detailed in Ireland et al. (2008).

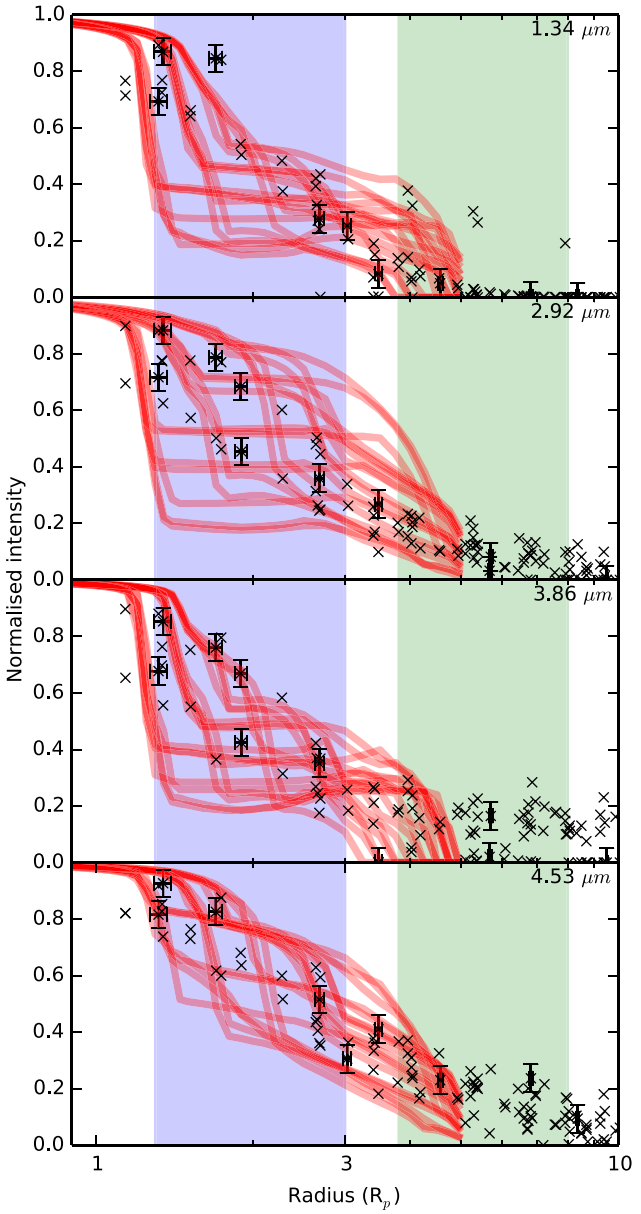

Figure 8. Brightness as a function of stellar radius. Data from model-independent brightness profiles recovered from observations are shown in black with representative error bars. CODEX profiles from the adjacent phase increments are shown in red, covering a range of pulsations cycles with widely varying atmospheric extension as demonstrated by the diversity of the profiles. The pale blue and green regions of the plots correspond in colour and radial extent to the inner two molecular shells identified in Fig. 3. The vertical axes are normalized intensity raised by some power to enhance the relevant information. This power in the first and third panels is 0.2 whilst for the second and fourth panels it is 0.4. The horizontal axis is in photospheric radii, which is 13 mas for the observations. (Stewart et al. 2013). The four panels are the different wavelength regions used in Fig. 6, and are labelled in their upper-right corners.

and 4.53 μm, it aligns with the measured outer H_2O layer, whilst at 1.34 and 3.86 μm this drop in intensity tends to occur within the outer 15 per cent of model, partially overlapping with the outer H_2O layer. The CO_2 layer identified in Section 4.1 is not predicted by the CODEX models as it occurs beyond the models' outer limit.

The observation data almost entirely fits within the broad range of possible spatial configurations predicted by the CODEX models. The vertical extent of the observation data emphasizes the degree of asymmetry which the stellar atmosphere exhibits, whilst each spherically symmetric CODEX phase increment follows a single curve. The observations generally align well with the more extended CODEX models within the inner two photospheric radii. Beyond this the observations are nearer to the compact models.

6 CONCLUSIONS

This paper concludes a series in which the novel use of *Cassini* observations of stellar occultations by the rings of Saturn for stellar science has been demonstrated and exploited to provide astrophysical insights. This technique offers a unique opportunity to obtain both spectral and high-resolution spatial information simultaneously, from far beyond the degrading effects caused by the atmosphere of the Earth.

Here, we presented a combination of spectral and spatial observations of Mira. Variations in the near-infrared spectrum of Mira through eight epochs of varying pulsation phase have been identified. Molecular atmospheric layers have been detected, with measurements of their relative sizes and molecular composition inferred from a set of three occultations obtained near $\phi \approx 0.1$. These structures are shown to dominate the tomographically recovered images obtained from these same observations. Temporal changes in these circumstellar structures have been observed over three epochs between Mira's visual and infrared maxima.

The state-of-the-art CODEX models have been rigorously assessed and found to be broadly consistent with the observations, with several notable discrepancies. The models and spectral observations were found to differ significantly in the epochs between the visual and infrared maxima, suggesting the molecular species and ratios used in the models are inaccurate. A comparison of the model-independent brightness profiles to the centre-to-limb profiles of the CODEX models shows a general good agreement the specific wavebands where key molecular features were identified. However, strong asymmetries were observed which the 1D models cannot predict. Spectral structures were identified in the observations which are not predicted by the CODEX models. This shows that there remain some inconsistencies with the CODEX models, giving them limited predictive ability in some spectral regions. These models could potentially be improved by revisiting the molecular species responsible for atmospheric absorption and the ratios between them, and to incorporate dust scattered flux as observed by Norris et al. (2012).

ACKNOWLEDGEMENTS

The authors would like to thank Michael Scholz for his valuable advice.

We acknowledge with thanks the variable star observations from the AAVSO International Database contributed by observers worldwide and used in this research

This publication makes use of data products from the Two Micron All Sky Survey, which is a joint project of the University of Massachusetts and the Infrared Processing and Analysis Center/California Institute of Technology, funded by the National Aeronautics and Space Administration and the National Science Foundation.

REFERENCES

Burns D. et al., 1998, MNRAS, 297, 462
Chandler A. A., Tatebe K., Wishnow E. H., Hale D. D. S., Townes C. H., 2007, ApJ, 670, 1347
Colwell J. E., Nicholson P. D., Tiscareno M. S., Murray C. D., French R. G., Marouf E. A., 2009, Saturn from Cassini Huygens. Springer, Berlin
Colwell J. E., Esposito L. W., Jerousek R. G., Sremčević M., Pettis D., Bradley E. T., 2010, AJ, 140, 1569
Cruzalebes P., Lopez B., Bester M., Gendron E., Sams B., 1998, A&A, 338, 132
Feroz F., Hobson M. P., Cameron E., Pettitt A. N., 2014, preprint (arXiv:1306.2144)
French R., 1993, Icarus, 103, 163
Hedman M. M., Nicholson P. D., Salo H., Wallis B. D., Buratti B. J., Baines K. H., Brown R. H., Clark R. N., 2007, AJ, 133, 2624
Höfner S., 2008, A&A, 491, L1
Ireland M. J., Scholz M., Tuthill P. G., Wood P. R., 2004, MNRAS, 355, 444
Ireland M. J., Scholz M., Wood P. R., 2008, MNRAS, 391, 1994
Ireland M. J., Scholz M., Wood P. R., 2011, MNRAS, 418, 114
Jerousek R. G., Colwell J. E., Esposito L. W., 2011, Icarus, 216, 280
Justtanont K., de Jong T., Tielens A. G. G. M., Feuchtgruber H., Waters L. B. F. M., 2004, A&A, 417, 625
Karovicova I., Wittkowski M., Boboltz D. A., Fossat E., Ohnaka K., Scholz M., 2011, A&A, 532, 1
Karovska M., Hack W., Raymond J., Guinan E., 1997, ApJ, 482, L175
Knapp G. R., Pourbaix D., Platais I., Jorissen A., 2003, A&A, 403, 993
Lockwood G. W., Wing R. F., 1971, ApJ, 169, 63
Lopez B. et al., 1997, ApJ, 488, 807
Martin D. C. et al., 2007, Nature, 448, 780
Matsuura M., Yamamura I., Cami J., Onaka T., Murakami H., 2002, A&A, 383, 972
Mauron N., Caux E., 1992, A&A, 265, 711
Mayer A. et al., 2011, A&A, 531, L4
Norris B. R. M. et al., 2012, Nature, 484, 220
Nowotny W., Aringer B., Höfner S., Lederer M. T., 2011, A&A, 529, A129
Sacuto S., Aringer B., Hron J., Nowotny W., Paladini C., Verhoelst T., Höfner S., 2010, A&A, 525, A42
Scholz M., Ireland M. J., Wood P. R., 2014, A&A, 565, A119
Skrutskie M. F. et al., 2006, AJ, 131, 1163
Stewart P. N., Tuthill P. G., Hedman M. M., Nicholson P. D., Lloyd J. P., 2013, MNRAS, 433, 2286 (Paper I)
Stewart P. N., Tuthill P. G., Nicholson P. D., Sloan G. C., Hedman M. M., 2015a, ApJS, 221, 30
Stewart P. N., Tuthill P. G., Nicholson P. D., Hedman M. M., Lloyd J. P., 2015b, MNRAS, 449, 1760 (Paper II)
Stewart P. N., Tuthill P. G., Monnier J. D., Ireland M. J., Hedman M. M., Nicholson P. D., Lacour S., 2015c, MNRAS, 455, 3102
Tej A., Lançon A., Scholz M., Wood P. R., 2003, A&A, 412, 481
Thompson R. R., Creech-Eakman M. J., Akeson R. L., 2002, ApJ, 570, 373
van Leeuwen F., 2007, A&A, 474, 653
van Loon J. T., Marshall J. R., Cohen M., Matsuura M., Wood P. R., Yamamura I., Zijlstra A. A., 2006, A&A, 447, 971
Wilson R. W., Baldwin J. E., Buscher D. F., Warner P. J., 1992, MNRAS, 257, 369
Winters J. M., Le Bertre T., Jeong K. S., Helling C., Sedlmayr E., 2000, A&A, 361, 641
Wittkowski M. et al., 2011, A&A, 532, L7
Woitke P., 2006a, A&A, 452, 537
Woitke P., 2006b, A&A, 460, L9
Woodruff H. C., Tuthill P. G., Monnier J. D., Ireland M. J., Bedding T. R., Lacour S., Danchi W. C., Scholz M., 2008, ApJ, 673, 418
Woodruff H. C. et al., 2009, ApJ, 691, 1328
Yamamura I., de Jong T., Cami J., 1999, A&A, 348, L55
Young J. S. et al., 2000, Proc. SPIE, 4006, 472

This paper has been typeset from a TEX/LATEX file prepared by the author.